Cascades of Parametric Instabilities in the Tokamak Plasma Edge during Electron Cyclotron Resonance Heating

A. Clod,[1] M. G. Senstius,[2] A. H. Nielsen,[1] R. Ragona,[1] A. S. Thrysøe,[1] U. Kumar,[3] S. Coda,[3] and S. K. Nielsen[1]

The TCV team[*]

[1]*Department of Physics, Technical University of Denmark, Fysikvej, DK-2800 Kongens Lyngby, Denmark*
[2]*Rudolf Peierls Centre for Theoretical Physics, University of Oxford, Oxford OX1 3NP, United Kingdom*
[3]*École Polytechnique Fédérale de Lausanne (EPFL), Swiss Plasma Center (SPC), CH-1015 Lausanne, Switzerland*

(Received 27 October 2023; accepted 27 February 2024; published 28 March 2024)

We report observations of nonlinear two-plasmon decay instabilities (TPDIs) of a high-power microwave beam, a process similar to half-harmonic generation in optics, during electron cyclotron resonance heating in a tokamak. TPDIs are found to occur regularly in the plasma edge due to wave trapping in density fluctuations for various confinement modes, and the frequencies of both observed daughter waves agree with modeling. Emissions from a cascade of subsequent decays, which indicate a generation of ion Bernstein waves, are correlated with fast-ion generation. This emphasizes the limitations of standard linear microwave propagation models and possibly paves the way for novel microwave applications in plasmas.

DOI: 10.1103/PhysRevLett.132.135101

Introduction.—Nonlinear parametric three-wave interactions can occur in media with a nonvanishing second-order nonlinear susceptibility if the intensity of an electromagnetic wave exceeds a threshold. Parametric interactions are extensively studied within the field of optics, where they are applied for, e.g., parametric amplification [1,2], second-harmonic generation [3,4], and half-harmonic generation [5]. Likewise, parametric decays of waves in plasmas, called parametric decay instabilities (PDIs) [6–9], have been suggested as a tool for THz generation in plasma-optical systems [10]. PDIs have also been observed in both ionospheric modification experiments [11–14] and in the solar atmosphere [15], and mitigation of PDIs is a critical issue for the high-power laser-plasma interactions [16–19] in inertial confinement fusion. High-power plasma waves generated by gyrotrons are applied for heating in magnetic confinement fusion (MCF) devices through electron cyclotron resonance heating (ECRH) [20,21]. During second harmonic ECRH, the power threshold required for a gyrotron beam to undergo a PDI is typically orders of magnitude above the gyrotron power [22]. Nevertheless, nonlinear backscattering with frequencies both up-shifted and down-shifted around the gyrotron frequency has been observed in second harmonic ECRH experiments at several medium-sized MCF devices [23–28]. This nonlinear backscattering has been connected to a degradation of microwave diagnostics [26], and a low-temperature laboratory experiment found a possibly connected irregular power absorption of 45% [29]. Additionally, multiple devices have independently reported on unexpected energetic ion generation [30,31] as well as ion cyclotron emissions [32] during second harmonic ECRH. All these events have been hypothesized to be caused by a series of low-threshold PDIs. An early theory predicts the nonlinear backscattering to be directly generated by a parametric decay of the gyrotron beam into a backscattered X-mode wave and a trapped ion Bernstein wave (IBW) [33]. This theory, however, could not produce the details of the observed backscattering spectrum [22]. Later theories instead predict the gyrotron beam to undergo an initial parametric decay into either two approximately half frequency upper hybrid (UH) waves that are trapped due to perturbations in the plasma density [22], denoted a two-plasmon decay instability (TPDI), or into one trapped UH wave and a backscattered X-mode wave [27]. The trapping of the UH waves makes the TPDI an absolute instability, and the resulting amplification of the UH daughter waves is predicted [34–39] to give rise to subsequent PDIs where the daughter UH waves decay into

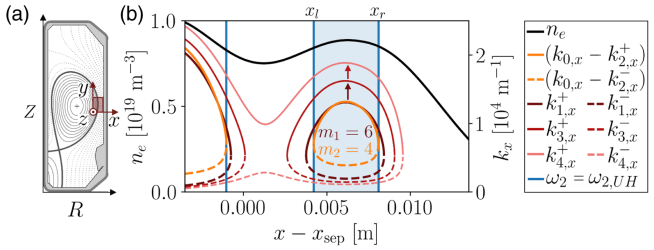

FIG. 1. (a) TCV cross section with global (R, Z) and local slab (x, y, z) coordinate systems where $\mathbf{e}_z \| \mathbf{B}^{(0)}$. (b) Example of the perpendicular wave number $k^{\pm}_{j,x}$ of two UH daughter waves with frequencies $f_1 = 41.27$ GHz, $f_2 = 41.43$ GHz that are trapped inside a density perturbation in the edge of a plasma with TCV parameters. The pump wave interacts with the daughter waves in the region $x \in [x_l, x_r]$ (blue) where both daughter waves propagate. Parameters are $T_e = 100$ eV and $B^{(0)} = B_0 R_0 / R$ with $B_0 = 1.43$ T and $R_0 = 0.88$ m. x_{sep} is positioned at $R = 1.08$ m. An UH-PDI of $k^{\pm}_{1,x}$ creates the downshifted trapped UH wave $k^{\pm}_{3,x}$ and an IBW (not plotted). A further UH-PDI of $k^{\pm}_{3,x}$ creates the free UH wave $k^{\pm}_{4,x}$.

a downshifted UH wave and an IBW as well as to recombination processes, creating the observed signals around the gyrotron frequency. The fraction of irregular power absorption due to this cascade of decays could range from 5% to as high as 80% in extreme cases [35,36,38]. Apart from directly reducing the ECRH efficiency and broadening the ECRH energy release profile [36], the energy transfer of the IBWs would result in a nonthermal ion distribution. As of now, broadband emissions around half gyrotron frequency have been reported [25], but conclusive evidence of TPDI daughter wave generation as well as a coupling to ion acceleration have not been observed.

In this Letter we present direct observations of primary TPDIs with two trapped daughter waves and a subsequent cascade of PDIs as well as a correlation between the subsequent PDIs and fast ion generation in the Tokamak à Configuration Variable (TCV) [40]. The identified TPDIs and subsequent parametric decays align with the predicted cascade in [34–38]. We show that TPDIs and subsequent parametric decays take place regularly in the plasma edge and demonstrate, additionally, that the observed daughter wave frequencies align with a TPDI model combined with a plasma turbulence simulation.

TPDI model.—To model the TPDI, we employ the local slab geometry illustrated in Fig. 1(a) and assume inhomogeneity of the plasma only along the x direction. A parametric decay of a pump wave $(\mathbf{k_0}, \omega_0)$ traveling in the x direction into two daughter waves $(\mathbf{k_1}, \omega_1)$, $(\mathbf{k_2}, \omega_2)$ becomes resonant if the selection rules

$$k_{0x} = k_{1,x} + k_{2,x} \qquad 0 = k_{1,y} + k_{2,y} \qquad 0 = k_{1,z} + k_{2,z}$$
$$\omega_0 = \omega_1 + \omega_2 \tag{1}$$

are satisfied. The TPDI can occur close to the second harmonic UH layer of a gyrotron beam polarized in X mode. The two daughter UH waves with approximately half the frequency of the gyrotron are thus created in the vicinity of their fundamental UH layer, and in this region they are nearly electrostatic and can be described by the local dispersion relation employed in [34,41]. This dispersion relation has the two branches; the forward propagating X-mode $(k^-_{\perp})$ and the backwards propagating electron Bernstein wave (EBW) $(k^+_{\perp})$, with $\perp$ being the direction perpendicular to the magnetic field. Because the dispersion relation depends on the plasma density, n_e, and background magnetic field strength, $B^{(0)}$, the selection rules [Eq. (1)] can only be satisfied in a local interaction region in an inhomogeneous plasma.

The TPDI occurs if the intensity of the pump wave is strong enough that the nonlinear coupling between the pump and daughter waves can overcome the losses of the two daughter waves, which are usually dominated by convection out of the interaction region. Therefore, if one or both of the daughter waves are spatially trapped around the interaction region, the instability becomes absolute, and the power threshold for TPDI to occur is severely reduced. Trapping of the daughter UH waves can occur if the plasma density is nonmonotonic with a local maximum in the vicinity of the second harmonic UH layer. In the scenario shown in Fig. 1(b), both primary daughter waves $k^{\pm}_{1,x}, k^{\pm}_{2,x}$ can propagate inside a cavity created by a density perturbation and are linearly converted between the forward propagating X-mode and backwards propagating EBW at their respective UH layers. After an initial period with exponential growth, the amplitude of the primary daughter waves exceeds the threshold for the onset of a secondary PDI into a downshifted UH wave $k^{\pm}_{3,x}$ and a free IBW. This class of PDI, denoted UH-PDI, is well known from both low-temperature plasmas [42] and MCF devices [20,43,44]. A cascade of UH-PDIs can continue until the frequency of the downshifted UH wave is low enough that the wave is no longer trapped, as seen in Fig. 1(b).

The eigenmodes that can propagate inside the 1D cavity are quantized by each having to satisfy the Bohr-Sommerfeld criterion

$$\int_{x_{l,j}}^{x_{r,j}} (|k^+_{j,x}| - |k^-_{j,x}|)\mathrm{d}x = (2m_j + 1)\pi, \qquad m_j \in \mathbb{Z}, \tag{2}$$

where m_j is the quantization number of the mode j. After employing a WKB description of the primary daughter waves, a second-order expansion of the nonlinear wave equation yields the coupled PDE system [25,34]

$$\mathrm{i}\frac{\partial C_1}{\partial t} + \sigma(C_1) = \nu_{12} \mathrm{e}^{-(y^2+z^2)/W^2} C_2^*$$
$$-\mathrm{i}\frac{\partial C_2^*}{\partial t} + \sigma(C_2)^* = \nu_{21}^* \mathrm{e}^{-(y^2+z^2)/W^2} C_1, \tag{3}$$

where C_j is a scaled WKB potential of daughter wave j, W is the width of the Gaussian gyrotron beam, and

$$\sigma(C_j) = \mathrm{i}\Gamma_j C_j + \mathrm{i}v_{jy}\frac{\partial C_j}{\partial y} - \Lambda_{jy}\frac{\partial^2 C_j}{\partial y^2} - \Lambda_{jz}\frac{\partial^2 C_j}{\partial z^2}, \quad (4)$$

contains linear damping Γ_j, convection losses in the y direction $v_{jy}\partial_y$, and diffraction losses $\Lambda_{jy}\partial_y^2$, $\Lambda_{jz}\partial_z^2$, all calculated with an averaging procedure as in [25]. The nonlinear coupling coefficients ν_{12}, ν_{21} take the form

$$\nu_{jj'} \propto \int_{x_l}^{x_r} \Upsilon(x) \mathrm{e}^{\mathrm{i}\int^x (k_{0,x} - k^+_{1,x} - k^+_{2,x})\mathrm{d}x'} \mathrm{d}x \quad (5)$$

where the integration bounds x_l, x_r are the overlapping region of the daughter waves (see Fig. 1) and $\Upsilon(x)$ depends on the background magnetic field, the plasma density, and the pump wave amplitude. The coupling coefficients $\nu_{jj'}$ depend on the wave number matching of the three waves, which is largest if the frequencies of the two primary daughter waves are slightly different. Equation (2) is satisfied by treating the poloidal wave number $k_{j,y}$ as a free parameter, and because the selection rules [Eq. (1)] require $k_{1,y} = -k_{2,y}$, only a finite number of frequency differences $\Delta\omega = \omega_2 - \omega_1$ are allowed. After evaluating the $\Delta\omega$ resulting in the largest nonlinear coupling, the system [Eq. (3)] is solved numerically on a grid with a second-order central difference scheme for space and a first-order forward difference scheme for time and periodic boundary conditions, yielding the instability growth rate γ, where $C_j \propto \exp(\gamma t)$. A complete model derivation and solution details are found in the Supplemental Material [45]. The saturation of the TPDI due to a subsequent cascade of decays is not modeled here, but simulations are found in, e.g., [37,39].

Experimental TPDI model validation.—To investigate predicted TPDIs, we installed a heterodyne radiometer with a transmission line at a launcher at an upper lateral port at TCV that employs a local oscillator frequency of 40.245 GHz and an 8-bit 5 GS/s digitizer (model M4x.2233-x4). A small WR-15 waveguide segment works as a high-pass filter, which limits the bandwidth of the radiometer to 41.1–42.2 GHz. The second harmonic ECRH system at TCV consists of three gyrotrons. One gyrotron, X2-1, has a frequency of 82.7 GHz and is positioned in the midplane at a toroidal position 23° away from the radiometer, and the two other gyrotrons, X2-4 and X2-5, both have a frequency of 83.8 GHz and are positioned at an identical toroidal position 116° away from the radiometer.

Figure 2(a) shows the trajectories of the X2-1 and X2-5 gyrotrons along with the radiometer (O mode) line of sight in an X2 heated deuterium plasma in TCV shot No. 77263 with $I_p = 0.11$ MA and $B_0 = 1.43$ T. The injected power and H_α signal are shown in Figs. 2(b) and 2(c). Until the neutral beam injection (NBI) is switched on at $t = 0.9$ s,

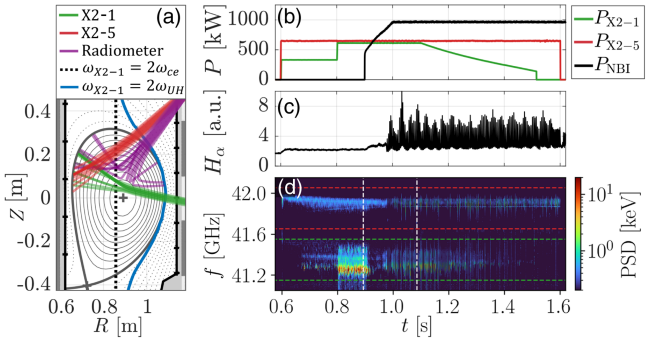

FIG. 2. (a) Resonances, gyrotron ray trajectories, and line of sight of the radiometer mapped to the poloidal cross section of TCV in shot No. 77263 at $t = 0.85$ s. (b),(c) Time traces of the injected power and H_α signal. (d) Frequency spectrum of the radiometer. The white dashed lines mark the time stamps t_0 in Fig. 3, and the red and green dashed lines mark bands around half gyrotron frequencies.

the plasma is in low-confinement mode (L mode) with turbulent plasma transport into the scrape-off layer (SOL). Afterwards, it transitions to high-confinement mode [46] (H mode), which is characterized by a buildup of a transport barrier and periodic bursts of filaments from edge-localized modes [47] (ELMs) that can be seen from the spikes in the H_α measurement. The radiometer spectrum in Fig. 2(d) shows a clear signal at half frequency of both the X2-1 gyrotron (green band) and X2-5 gyrotron (red band) with different characteristics in the L-mode and H-mode phases of the shot. The timing of the two signals is correlated with the switch-on of the gyrotrons, and the power spectral density (PSD) of the signal at $f \approx f_{X2\text{-}1}/2$ scales nonlinearly with the power of the X2-1 gyrotron when it is increased at $t = 0.8$ s. Examples of two radiometer acquisitions taken during times in the L mode and H mode, respectively, are shown in Fig. 3. In both acquisitions the signal consists of short events with two individual modes centered around exactly half the frequency of the X2-1 gyrotron, which suggests that they indeed result from TPDIs of the X2-1 beam. During the L mode the events occur regularly, whereas they are

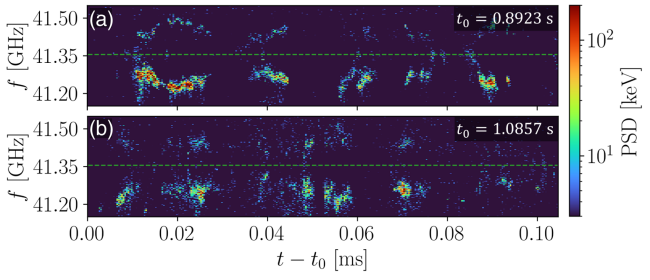

FIG. 3. Time trace of the radiometer frequency spectrum at a time (a) during L mode, and (b) during an ELM event in H mode in shot No. 77263. The green line marks $f = f_{X2\text{-}1}/2$.

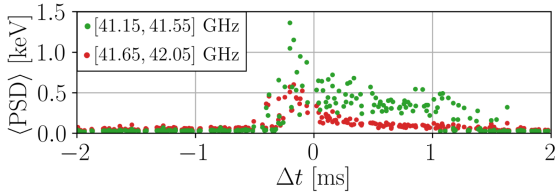

FIG. 4. Average PSD in each of the frequency bands marked in Fig. 2(d) vs the time difference between the acquisition and the closest peak in the H_α signal in shot No. 77263 during the H-mode period $t \in [0.98, 1.11]$ s with constant gyrotron power.

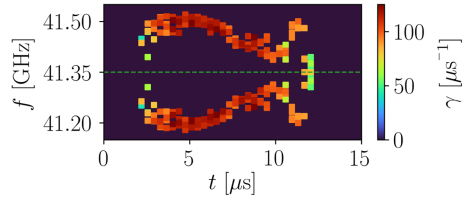

FIG. 6. Daughter wave frequencies and growth rates predicted by the 1D TPDI model in Eqs. (1)–(5) for the blob structure shown in Fig. 5. Only data from the four poloidal positions with highest instability growth rate are shown.

grouped in short temporal periods of ∼1 ms during the H mode with zero signal in between.

The large density perturbations occurring due to ejected plasma filaments during ELM events can cause trapping of half-frequency UH waves, which facilitates TPDIs in the plasma edge. Figure 4 shows a clear correlation between the timing of ELMs and the spikes in the PSD of the TPDI signal from both gyrotrons during the H-mode phase of the shot, which validates that TPDIs take place during ELMs. This is consistent with earlier experiments [25].

During the L mode, turbulent blob filaments erupt from the plasma core into the SOL [48]. These blob structures cause trapping of UH daughter waves as well. To obtain realistic estimates of the density and temperature in the plasma edge in shot No. 77263, a simulation is carried out with the 2D interchange turbulence code HESEL [49,50] with parameters based directly on Thomson scattering measurements [51] at $t = 0.85$ s and with drift waves excluded to ensure that the simulation stays in the L mode. As seen in Fig. 5, the density of a blob can perturb the position of the second harmonic UH resonance enough to support trapping of TPDI daughter waves in the radial direction. We predict the resulting TPDI growth rates and daughter wave frequencies by solving the model in Eqs. (1)–(5) with a local slab geometry [see Fig. 1(a)], where the density inhomogeneity is only included along radial 1D cuts, taken every 0.6 mm in the poloidal direction within a gyrotron width. Figure 6 shows the resulting primary daughter wave frequencies and growth rates as a function of time. The frequency shift of the daughter waves depends on the blob position, as eigenmodes with larger quantization numbers are trapped when the blob is closer to the plasma core. Naturally, different blob structures give rise to TPDIs with different features. Generally, larger blobs are found to result in more separated daughter wave frequencies and larger instability growth rates in this parameter range. The predicted daughter waves show a good resemblance with typical events in the signal measured in the L mode [Fig. 3(a), 0.01 ms to 0.02 ms] with similar frequency shifts and temporal signal lengths. Thus, the observed signals during the L mode are consistent with TPDIs in the plasma edge.

In the TCV L-mode shot No. 77585 with a limiter plasma with $I_p = 0.085$ MA and $B_0 = 1.48$ T, the primary daughter waves from TPDI of the X2-5 gyrotron were observed at $f \sim 41.9$ GHz along with two downshifted signals as seen in Figs. 7(c) and 7(d). The frequency shifts of 0.4 GHz and 0.8 GHz match one and two lower hybrid (LH) wave frequencies, respectively, firmly suggesting that the signals are daughter waves from subsequent UH-PDIs of the primary daughter waves into a downshifted UH wave

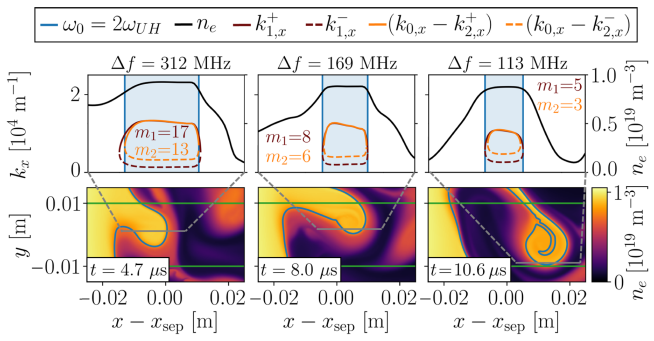

FIG. 5. Edge density simulated by HESEL at three time stamps around $t = 0.85$ s in No. 77263. The gray lines mark the 1D trapping regions that result in the largest instability growth rate within a gyrotron width (green lines). The corresponding trapped eigenmodes are plotted in the figures above.

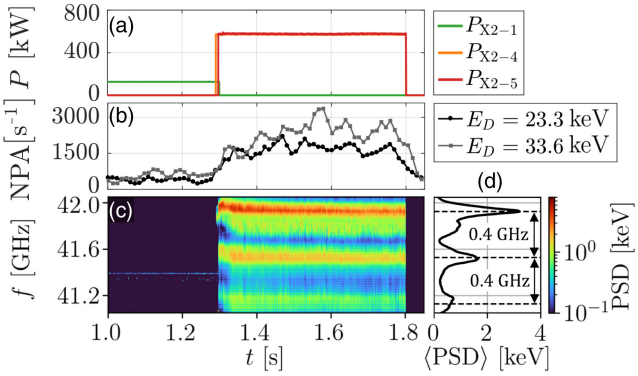

FIG. 7. Time traces of (a) the injected power, (b) the NPA counts of high energy deuterium neutrals, and (c) a of the radiometer in shot No. 77585. (d) Smoothed average PSD in the spectrum for $t \in [1.4\text{ s}, 1.5\text{ s}]$.

and an IBW on the LH wave branch. Figure 7(b) shows the counts of a neutral particle analyzer (NPA) of high-energy deuterium neutrals. The counts increase considerably in the period where the X2-4 and X2-5 gyrotrons are switched on and TPDIs and UH-PDIs are occurring, which indicates a generation of suprathermal ions. This observation implies that IBWs are generated in subsequent UH-PDIs, as predicted in [34–38].

In summary, TPDIs are found to occur regularly in the plasma edge in the TCV tokamak during both L-mode and H-mode operation due to trapping of the daughter waves in density fluctuations created by blobs and ELMs, respectively. The observed daughter wave frequencies are shown to be consistent with a TPDI model combined with a plasma turbulence simulation with parameters directly based on TCV diagnostics. The identified daughter waves generated in both TPDIs and a subsequent cascade of UH-PDIs as well as observations of a correlation between the cascading parametric decays and a suprathermal ion generation all align with recent predictions [34–38]. If consequences of the TPDIs and subsequent decays are found to be critical, they could be mitigated by either operating in a mode where most density fluctuations in the plasma edge are small enough to prevent trapping of two half frequency UH waves or by moving the gyrotron launch positions away from the midplane, as this would generally give rise to smaller density fluctuations along the paths of the gyrotron beams.

The presented measurements of parametric instabilities during second-harmonic heating underline the importance of understanding the limits of linear microwave propagation models as we progress towards fusion-relevant devices like the experimental reactors ITER and DEMO. In particular, another nonlinear decay process that has recently been proposed to occur during fundamental O-mode heating [52] remains untested.

This work has been supported by research Grant No. 15483 from VILLUM FONDEN and by the Carlsberg Foundation, Grant No. CF23-0181. This work has been carried out within the framework of the EUROfusion Consortium, partially funded by the European Union via the Euratom Research and Training Programme (Grant Agreement No. 101052200—EUROfusion). The Swiss contribution to this work has been funded by the Swiss State Secretariat for Education, Research and Innovation (SERI). Views and opinions expressed are however those of the authors only and do not necessarily reflect those of the European Union, the European Commission or SERI. Neither the European Union nor the European Commission nor SERI can be held responsible for them. This work was supported in part by the Swiss National Science Foundation.

[*] See the author list of H. Reimerdes *et al.*, 2022 Nucl. Fusion 62 042018.
[1] J. Riemensberger, N. Kuznetsov, J. Liu, J. He, R. N. Wang, and T. J. Kippenberg, Nature (London) **612**, 56 (2022).
[2] B.-U. Sohn, Y.-X. Huang, J. W. Choi, G. F. R. Chen, D. K. T. Ng, S. A. Yang, and D. T. H. Tan, Nat. Commun. **13**, 7218 (2022).
[3] I. Abdelwahab *et al.*, Nat. Photonics **16**, 644 (2022).
[4] G. Q. Ngo *et al.*, Nat. Photonics **16**, 769 (2022).
[5] A. Marandi, K. A. Ingold, M. Jankowski, and R. L. Byer, Optica **3**, 324 (2016).
[6] D. F. DuBois, and M. V. Goldman, Phys. Rev. Lett. **14**, 544 (1965).
[7] M. Porkolab, and R. P. H. Chang, Phys. Rev. Lett. **22**, 826 (1969).
[8] M. N. Rosenbluth, Phys. Rev. Lett. **29**, 565 (1972).
[9] A. D. Piliya, JETP Lett. **17**, 266 (1973), http://jetpletters.ru/ps/1541/article_23571.shtml.
[10] M. Singh and R. P. Sharma, Contrib. Plasma Phys. **53**, 540 (2013).
[11] B. Thidé, H. Kopka, and P. Stubbe, Phys. Rev. Lett. **49**, 1561 (1982).
[12] A. Samimi, W. A. Scales, H. Fu, P. A. Bernhardt, S. J. Briczinski, and M. J. McCarrick, J. Geophys. Res. Space Phys. **118**, 502 (2013).
[13] H. Y. Fu *et al.*, Geophys. Res. Lett. **47**, e2020GL089747 (2020).
[14] B. Eliasson *et al.*, Nat. Commun. **12**, 6209 (2021).
[15] M. Hahn, X. Fu, and D. W. Savin, Astrophys. J. **933**, 52 (2022).
[16] J. Zhang, J. F. Myatt, R. W. Short, A. V. Maximov, H. X. Vu, D. F. DuBois, and D. A. Russell, Phys. Rev. Lett. **113**, 105001 (2014).
[17] R. K. Follett *et al.*, Phys. Rev. Lett. **116**, 155002 (2016).
[18] R. K. Follett, J. G. Shaw, J. F. Myatt, J. P. Palastro, R. W. Short, and D. H. Froula, Phys. Rev. Lett. **120**, 135005 (2018).
[19] D. Turnbull, A. V. Maximov, D. H. Edgell, W. Seka, R. K. Follett, J. P. Palastro, D. Cao, V. N. Goncharov, C. Stoeckl, and D. H. Froula, Phys. Rev. Lett. **124**, 185001 (2020).
[20] H. P. Laqua, V. Erckmann, H. J. Hartfuß, and H. Laqua, Phys. Rev. Lett. **78**, 3467 (1997).
[21] R. Prater *et al.*, Nucl. Fusion **48**, 035006 (2008).
[22] A. Yu Popov and E. Z. Gusakov, Plasma Phys. Controlled Fusion **57**, 025022 (2015).
[23] E. Westerhof *et al.* (The TEXTOR Team), Phys. Rev. Lett. **103**, 125001 (2009).
[24] S. K. Nielsen, M. Salewski, E. Westerhof, W. Bongers, S. B. Korsholm, F. Leipold, J. W. Oosterbeek, D. Moseev, and M. Stejner, Plasma Phys. Controlled Fusion **55**, 115003 (2013).
[25] S. K. Hansen, S. K. Nielsen, J. Stober, J. Rasmussen, M. Stejner, M. Hoelzl, and T. Jensen, Nucl. Fusion **60**, 106008 (2020).
[26] S. K. Hansen, A. S. Jacobsen, M. Willensdorfer, S. K. Nielsen, J. Stober, K. Höfler, M. Maraschek, R. Fischer, and M. Dunne, Plasma Phys. Controlled Fusion **63**, 095002 (2021).
[27] A. Tancetti *et al.*, Nucl. Fusion **62**, 074003 (2022).

[28] A. Tancetti *et al.*, Plasma Phys. Controlled Fusion **65**, 015001 (2023).
[29] A. B. Altukhov, V. I. Arkhipenko, A. D. Gurchenko, E. Z. Gusakov, A. Yu. Popov, L. V. Simonchik, and M. S. Usachonak, Europhys. Lett. **126**, 15002 (2019).
[30] S. Coda and The TCV Team, Nucl. Fusion **55**, 104004 (2015).
[31] M. Martínez, B. Zurro, A. Baciero, D. Jiménez-Rey, and V. Tribaldos, Plasma Phys. Controlled Fusion **60**, 025024 (2018).
[32] S. Sumida, K. Shinohara, M. Ichimura, T. Bando, A. Bierwage, T. Kobayashi, H. Yamazaki, S. Moriyama, and S. Ide, Plasma Phys. Controlled Fusion **65**, 075002 (2023).
[33] E. Z. Gusakov and A. Y. Popov, Phys. Rev. Lett. **105**, 115003 (2010).
[34] E. Z. Gusakov and A. Y. Popov, Phys. Plasmas **23**, 082503 (2016).
[35] E. Z. Gusakov and A. Y. Popov, Plasma Phys. Controlled Fusion **60**, 025001 (2017).
[36] E. Z. Gusakov and A. Y. Popov, Nucl. Fusion **59**, 104003 (2019).
[37] E. Z. Gusakov, A. Yu Popov, and P. V. Tretinnikov, Nucl. Fusion **59**, 106040 (2019).
[38] E. Z. Gusakov and A. Y. Popov, Plasma Phys. Controlled Fusion **62**, 025028 (2020).
[39] M. G. Senstius, E. Z. Gusakov, A. Yu Popov, and S. K. Nielsen, Plasma Phys. Controlled Fusion **64**, 115001 (2022).
[40] H. Reimerdes *et al.*, Nucl. Fusion **62**, 042018 (2022).
[41] S. K. Hansen, S. K. Nielsen, and J. Stober, Phys. Plasmas **30**, 042103 (2023).
[42] S. Hiroe, and H. Ikegami, Phys. Rev. Lett. **19**, 1414 (1967).
[43] F. S. McDermott, G. Bekefi, K. E. Hackett, J. S. Levine, and M. Porkolab, Phys. Fluids **25**, 1488 (1982).
[44] S. K. Hansen, S. K. Nielsen, J. Stober, J. Rasmussen, M. Salewski, and M. Stejner, Phys. Plasmas **26**, 062102 (2019).
[45] See Supplemental Material at http://link.aps.org/supplemental/10.1103/PhysRevLett.132.135101 for a complete model derivation and details on the numerical solution.
[46] F. Wagner *et al.*, Phys. Rev. Lett. **53**, 1453 (1984).
[47] H Zohm, Plasma Phys. Controlled Fusion **38**, 105 (1996).
[48] O. E. Garcia *et al.*, Plasma Phys. Controlled Fusion **48**, L1 (2005).
[49] A. H. Nielsen *et al.*, Plasma Phys. Controlled Fusion **59**, 025012 (2017).
[50] A. H. Nielsen *et al.*, Nucl. Fusion **59**, 086059 (2019).
[51] H. Arnichand *et al.*, J. Instrum. **14**, C09013 (2019).
[52] E. Z. Gusakov and A. Y. Popov, Phys. Rev. Lett. **128**, 065001 (2022).